

Influence of Cluster Configurations and Nucleon–Nucleon Scattering Cross-Section on Stopping Power in Heavy-Ion Collisions

S. Y. Yao (姚少雨),¹ X. G. Deng (邓先概) ^{1,2,*} and Y. G. Ma (马余刚) ^{1,2,†}

¹*Key Laboratory of Nuclear Physics and Ion-beam Application (MOE),
Institute of Modern Physics, Fudan University, Shanghai 200433, China*

²*Shanghai Research Center for Theoretical Nuclear Physics, NSFC and Fudan University, Shanghai 200438, China*

(Dated: August 19, 2025)

We investigate the impacts of nuclear α -clustering structures and nucleon–nucleon cross-section on nuclear stopping power for $^{16}\text{O} + ^{40}\text{Ca}$ collisions below 300 MeV/nucleon using an extended quantum molecular dynamics (EQMD) model. Our results show that the specific α -clustering configurations of ^{16}O —including chain, square, kite, and tetrahedron—have a significant effect on collision dynamics. Among them, the tightly bound tetrahedral structure exhibits the highest stopping power. Moreover, the repulsive Coulomb interaction is found to reduce the stopping power of protons in the Fermi-energy domain. At higher energies, the decreasing trend is influenced by both the nucleon–nucleon cross-section and the mean field.

PACS numbers: 25.70.-z, 24.10.Lx, 21.30.Fe

I. INTRODUCTION

Heavy ion collisions (HICs) provide a venue for studying the properties of nuclear matter under different thermal and dense conditions, offering insights into the equation of state (EOS) and transport properties of nuclear matter [1–8], particularly in intermediate- and high-energy collisions. Stopping power [9–11], collective flow [12, 13], and fragmentation [14, 15] are crucial indicators of nuclear system evolution during collisions, revealing mechanisms of energy dissipation and momentum transfer [14, 16–20]. These observables also provide essential constraints on transport models, especially for intermediate- and high-energy nuclear reactions [18, 21]. A key observable for studying stopping power in HICs is the isotropy ratio R_E , which measures the redistribution of energy from longitudinal to transverse direction during the collision. Another observable, introduced by the FOPI collaboration, is the transverse-to-longitudinal variance ratio (vartl), which reflects the relative anisotropy of the particle distribution, indicating the degree of stopping and the thermalization in nuclear systems [22]. This observable has been widely used by experimental collaborations such as INDRA and ALADIN to analyze nuclear stopping at moderate energies [9, 23]. It is found that the stopping power observable is correlated with the amount of side flow [22, 24] as well as the magnetic field and eccentricity [25]. In the Fermi-energy domain, these observables are sensitive to the in-medium nucleon–nucleon cross-section in nuclear matter [11, 23, 26, 27].

In recent years, there has been growing interest in the impact of initial geometric fluctuations in intermediate-energy heavy-ion reactions [28–31] as well as in relativistic heavy-ion collisions [32–46]. Meanwhile, experimental

studies at the Relativistic Heavy Ion Collider (RHIC) have revealed structural deformation characteristics of atomic nuclei [47–49]. Therefore, it is essential to explore nuclear structure information using different observables in the moderate reaction energy ranges. On the one hand, this deepens our understanding on nuclear structure information, especially for clustering configurations (e.g., tetrahedron vs. chain of ^{16}O) on nuclear matter properties. In some previous literature, it is shown that clustering at low density has significant effects on astrophysical nuclear equations of state [50, 51]. On the other hand, it enables mutual validation, using different observables and/or different models. Therefore, in this work, we employ the extended quantum molecular dynamics (EQMD) model to study nuclear stopping power by simulating collisions between α -cluster structured ^{16}O projectiles and normally structured ^{40}Ca target nuclei. We explore different α -clustering configurations of ^{16}O , including chain, square, kite, and tetrahedral structures, to assess their impacts on energy dissipation and stopping observables. Additionally, we investigate the impact of various nucleon–nucleon cross-sections on stopping power observables, examining how cross-section choices affect isotropy and collision dynamics.

The paper is organized as follows: Section II introduces the models and analysis methods in this work. Section III explores two factors: the role of the Coulomb potential in stopping and a comparison of stopping behaviors for different collision cross sections. Finally, the summary and conclusions are presented in Sec. IV.

II. MODEL INTRODUCTIONS AND ANALYSIS METHOD

A. EQMD model

The extended quantum molecular dynamics model [52] is a sophisticated approach used in the simulation of

* xiangai.deng@fudan.edu.cn

† mayugang@fudan.edu.cn

heavy-ion collisions. It extends the traditional quantum molecular dynamics model by allowing greater flexibility in the description of nucleon wave packets, which makes it particularly useful for investigating the dynamics of nuclear matter at moderate energies. Unlike the standard QMD model [4, 53], which assumes constant widths for nucleon wave packets, EQMD introduces dynamically varying widths that allow for a more accurate representation of nucleon interactions and correlations. Some developments for the EQMD model are also reported in Refs. [54–56].

In EQMD, nucleons (both protons and neutrons) are represented as Gaussian wave packets. The nucleon's wave function is a Gaussian with time-dependent width. The total system's wave function can be described as a product of individual nucleon wave functions [52]:

$$\Psi = \prod_i \phi_i(\mathbf{r}_i), \quad (1)$$

where $\phi_i(\mathbf{r}_i)$ is the wave function of the i -th nucleon. The Gaussian form of each nucleon's wave function is given by:

$$\phi_i(\mathbf{r}_i) = \left(\frac{v_i + v_i^*}{2\pi} \right)^{3/4} \exp \left[-\frac{v_i}{2} (\mathbf{r}_i - \mathbf{R}_i)^2 + \frac{i}{\hbar} \mathbf{P}_i \cdot \mathbf{r}_i \right], \quad (2)$$

where R_i and P_i denote the nucleon's position and momentum centers in phase space. The width v_i is a complex quantity, given by $v_i = \frac{1}{\lambda_i} + i\delta_i$, with λ_i being the real part related to the spatial extension of the wave packet, and δ_i the imaginary part describing its phase evolution. The real part λ_i must be positive to ensure a valid physical nucleon density.

The probability or density distribution for each nucleon has a Gaussian form, expressed as:

$$\rho_i(\mathbf{r}) = \frac{1}{(\pi\lambda_i)^{3/2}} \exp \left[-\frac{(\mathbf{r} - \mathbf{R}_i)^2}{\lambda_i} \right]. \quad (3)$$

This formula shows that the spatial distribution of a nucleon depends on its position center R_i and the dynamically evolving width λ_i . Allowing λ_i to change over time makes EQMD a flexible and adaptable model for capturing nuclear dynamics during collisions.

The Hamiltonian of the system, which governs its dynamics, can be written as:

$$\begin{aligned} H &= \langle \Psi | \sum_i \left(-\frac{\hbar^2}{2m} \nabla_i^2 - \hat{T}_{\text{c.m.}} \right) + \hat{H}_{\text{int}} | \Psi \rangle \\ &= \sum_i \left(\frac{\mathbf{P}_i^2}{2m} + \frac{3\hbar^2}{2} \frac{1 + \lambda_i^2 \delta_i^2}{2m\lambda_i} - T_{\text{c.m.}} \right) + H_{\text{int}}, \end{aligned} \quad (4)$$

where $\hat{T}_{\text{c.m.}}$ is the zero-point kinetic energy due to the center-of-mass motion, and \hat{H}_{int} represents the potential interactions between nucleons.

The effective interaction H_{int} is described by

$$H_{\text{int}} = H_{\text{Sky.}} + H_{\text{Coul.}} + H_{\text{Symm.}} + H_{\text{Pauli}}, \quad (5)$$

where $H_{\text{Sky.}}$, $H_{\text{Coul.}}$, $H_{\text{Symm.}}$, and H_{Pauli} represent the Skyrme, Coulomb, symmetry, and Pauli potentials, respectively. The Skyrme potential, consisting of two-body and three-body terms, is:

$$H_{\text{Sky.}} = \frac{\alpha}{2\rho_0} \int \rho^2(\mathbf{r}) d\mathbf{r} + \frac{\beta}{(\gamma+1)\rho_0^\gamma} \int \rho^{\gamma+1}(\mathbf{r}) d\mathbf{r}, \quad (6)$$

where α , β , and γ are parameters associated with the incompressibility of the nuclear equation of state. In this work, we use $\alpha = -124.3$ MeV, $\beta = 70.5$ MeV, $\gamma = 2$. At saturation density of nuclear matter $\rho_0 = 0.16$ fm⁻³, binding energy per nucleon E/A and the incompressibility K are -16.5 MeV and 380 MeV, respectively. The symmetry potential, simplified, is

$$H_{\text{Symm.}} = \frac{c_s}{2\rho_0} \int (\rho_p - \rho_n)^2 d\mathbf{r}, \quad (7)$$

where ρ_p and ρ_n denote proton and neutron densities, respectively. The symmetry energy coefficient is taken as $c_s = 25$ MeV. The Coulomb potential considers only the direct term and is given by

$$H_{\text{Coul.}} = \frac{\alpha_0}{2} \int d\mathbf{r} d\mathbf{r}' \frac{\rho_p(\mathbf{r})\rho_p(\mathbf{r}')}{|\mathbf{r} - \mathbf{r}'|}. \quad (8)$$

with α_0 being the fine structure constant. Finally, the Pauli potential reflects the Fermi nature of nucleons and is

$$H_{\text{Pauli}} = \frac{c_P}{2} \sum_i (f_i - f_0)^\mu \theta(f_i - f_0). \quad (9)$$

Here, f_i is the overlap of the i -th nucleon with other nucleons having the same spin and isospin, i.e., $f_i \equiv \sum_j \delta(S_i, S_j) \delta(I_i, I_j) |\langle \phi_i | \phi_j \rangle|^2$, and θ is the unit step function. The parameters are set as $c_P = 15$ MeV, $f_0 = 1.0$, and $\mu = 1.3$. This Pauli potential inhibits the system to collapse into the Pauli-blocked state at low energy and gives the model the capability to describe α -particle clustering [57]. This capability is very important for our calculation because it gives us the possibility to extract information about clustering configurations from the nuclear stopping.

In the model, the equations of motion for the nucleons can be written as [52]

$$\begin{aligned} \dot{\mathbf{R}}_i &= \frac{\partial H}{\partial \mathbf{P}_i}, & \dot{\mathbf{P}}_i &= -\frac{\partial H}{\partial \mathbf{R}_i}, \\ \frac{3\hbar}{4} \dot{\lambda}_i &= -\frac{\partial H}{\partial \delta_i}, & \frac{3\hbar}{4} \dot{\delta}_i &= \frac{\partial H}{\partial \lambda_i}. \end{aligned} \quad (10)$$

These equations describe the time evolution of the nucleon position, momentum, and wave packet width parameters during the heavy-ion collision process. In the model, the cross section σ_{NN} is energy-dependent nucleon-nucleon collision cross section parametrized as [52],

$$\sigma_{NN} = \frac{100}{1 + \epsilon'/200 \text{ MeV}} \text{ mb}, \epsilon' = p_{\text{rel}}^2/2m, \quad (11)$$

where p_{rel} is relative momentum. The collision is assumed to be isotropic. The collision process in the simulation is mainly handled through three components: the reaction channel, the nucleon-nucleon cross-section, and the Pauli blocking mechanism. Specifically, two nucleons are considered to undergo a collision during a time step Δt if their minimum relative distance d_{min} satisfies $d_{min} \leq d_0 = \sqrt{(\sigma_{NN}/\pi)}$. After satisfying the geometric condition, the Pauli blocking criterion is further applied to ensure the quantum statistical property of the system.

The phase space of nucleons is obtained initially from a random configuration. To get the energy-minimum state as a ground state, a frictional cooling method is used for the initialization process [52, 57]. The EQMD model can describe the ground state properties, such as binding energy, rms radius, and deformation, etc., quite well over a very wide mass range.

B. GEMINI++

The deexcitation of hot nuclear fragments produced in heavy-ion collisions is a critical process for understanding the final state of the system [58]. To accurately model this process, we employ the GEMINI++ code [59, 60], which is an improved version of the GEMINI model developed by Charity [61]. GEMINI++ is a Monte Carlo simulation tool designed to handle various decay modes, including light-particle evaporation and symmetric fission [60, 61]. Following the initial evolution of nuclear interactions simulated by the EQMD model, hot fragments are generated, each characterized by its charge number Z , mass number A , and excitation energy E^* . The EQMD code halts when the excitation energy of the heaviest fragments falls below a specified threshold E_{stop} .

If the excitation energy is greater than zero, the sequential decays of the prefragments are simulated using the GEMINI++ code. The decay width for the emission of a light particle (Z_i, A_i) with spin S_i from a system (Z_0, A_0) with excitation energy E^* and spin S_{CN} , leaving a residual system (Z_d, A_d) with spin S_d , is calculated using the Hauser-Feshbach formalism [62]:

$$\Gamma_i^{HF} = \frac{1}{2\pi\rho_0} \int d\epsilon \sum_{S_d=0}^{+\infty} \sum_{J=|S_{CN}-S_d|}^{S_{CN}+S_d} \sum_{l=|J-S_i|}^{J+S_i} T_l(\epsilon) \rho(U, S_d), \quad (12)$$

where ϵ is the kinetic energy of the emitted particle, J is the total angular momentum, and $T_l(\epsilon)$ is the transmission coefficient or barrier penetration factor. The thermal excitation energy U is given by

$$U = E^* - E_{rot} - B_i - \epsilon, \quad (13)$$

where E_{rot} is the rotational energy of the ground-state configuration, and B_i is the separation energy calculated from nuclear mass tables.

To model the nuclear level densities, we adopt the stan-

dard Fermi-gas model:

$$\rho(E^*, J) \propto (2J+1) \frac{\exp\left[2\sqrt{a(E^* - E_1)}\right]}{a^{1/4}(E^* - E_1)^{5/4}}, \quad (14)$$

where a is the level-density parameter and E_1 is the energy backshift, both of which are treated as free parameters that account for shell effects.

The level-density parameter a is expressed as [63]:

$$a = [0.127 + 0.00498(S(Z, N) - \delta') - 0.0000895A]A, \quad (15)$$

where

$$\delta' = \begin{cases} +0.5P_d, & \text{even-even nuclei} \\ 0, & \text{odd-A nuclei} \\ -0.5P_d, & \text{odd-odd nuclei.} \end{cases} \quad (16)$$

The deuteron pairing energy P_d is computed from experimental mass tables as:

$$P_d = \frac{1}{2}(-1)^Z [-M_{exp}(A+2, Z+1) + 2M_{exp}(A, Z) - M_{exp}(A-2, Z-1)], \quad (17)$$

where M_{exp} represents the experimental mass of the nucleus. The derivative of the shell correction energy $S(Z, N)$ with respect to mass number A is approximated using finite differences:

$$\frac{dS(Z, N)}{dA} = \frac{S(Z+1, N+1) - S(Z-1, N-1)}{4}. \quad (18)$$

Using these formulations, GEMINI++ provides a comprehensive framework for simulating the de-excitation of nuclear fragments, leading to insights into the production mechanisms of heavy fragments in nuclear reactions. More details can be found in Ref. [63].

C. Nuclear stopping

To describe nuclear stopping power, we use the ratio of beam energy transferred to the parallel direction, R_E , which is expressed as Ref. [9]:

$$R_E = \frac{\sum E_{\perp}}{2\sum E_{\parallel}}, \quad (19)$$

where E_{\perp} (E_{\parallel}) is the transverse (parallel) kinetic energy of the fragments in the center-of-mass system. This ratio effectively reflects the isotropic characteristics of nuclear reactions. Specifically, if $R_E < 1$, it indicates partial transparency; when $R_E = 1$, it represents full stopping; and if $R_E > 1$, it indicates super-stopping.

Furthermore, $vartl$, first proposed by the FOPI Collaboration [22], is defined as the ratio of variances of transverse and parallel rapidity distributions. The variance is

calculated as the average over multiple events. Its expression is

$$\text{var}t_l = \left\langle \frac{\sigma(y_\perp)}{\sigma(y_\parallel)} \right\rangle = \left\langle \frac{\sqrt{\frac{1}{N} \sum_{i=1}^N (y_{\perp,i} - \langle y_\perp \rangle)^2}}{\sqrt{\frac{1}{N} \sum_{i=1}^N (y_{\parallel,i} - \langle y_\parallel \rangle)^2}} \right\rangle, \quad (20)$$

where $\sigma(y_\perp)$ and $\sigma(y_\parallel)$ represent the variances of transverse and parallel rapidity distributions, respectively. If the nuclear collision is fully stopped, the rapidity distribution will be isotropic. In the calculations of R_E and $\text{var}t_l$, we did not strictly follow the formulas on an event-by-event basis. It was observed that computing R_E for each individual event led to fluctuations in the results, especially at lower energy ranges with fewer free nucleons emitted. To avoid this issue, we averaged R_E over 100 events. For Figs. 5 and 6, since fragment information is not available, we calculated R_E in nucleon space.

III. RESULTS AND DISCUSSION

In the EQMD model, the first essential step of collision simulation is to construct a physically reasonable initial nucleus. This initialization is typically achieved through frictional cooling, in which a dissipation term is introduced during the dynamical evolution to gradually reduce the system's kinetic energy, eventually reaching a stable state with minimal internal energy. After the cooling process, the resulting ^{16}O nucleus exhibits an average binding energy of -7.91 MeV per nucleon (chain: -7.82 MeV, kite: -7.79 MeV, square: -7.92 MeV, and tetrahedron: -7.82 MeV), which is very close to the experimental ground-state value of -7.98 MeV. Here we did not specify any of these configurations as the ground state of ^{16}O since their binding energies are close to each other, in particular, we aim to compare different α -clustering configuration effects in the present work. We also note that the binding energies obtained here differ from those reported in the previous literature [64], mainly because the parameter C_p used in the present work is 15 MeV, whereas a value of 20 MeV was adopted in that reference. The Pauli potential plays a crucial role in this process. By suppressing the collapse of the system into Pauli-blocked states at low energies, it enables the model to naturally form α clusters [57, 65–68]. For ^{16}O , different structural configurations naturally emerge during cooling process and then can be classified as chain, square, kite, or tetrahedral shapes. In contrast, with the increase of the nucleon number of atomic nuclei, the nucleus, e.g., ^{40}Ca in this work, is more random without specific structural patterns and is therefore treated as a spherical nucleus.

Through the EQMD model, we studied the effects of α -clustering structure of ^{16}O , including chain, square, kite, and tetrahedron on the nuclear stopping. Since ^{16}O rotates uniformly around its central axis during the collision, we can roughly order its nuclear density distribu-

tion in the beam direction as chain $<$ kite $<$ square $<$ tetrahedron. After the collision, we selected fragments with excitation energy greater than 0 and mass number greater than 4 to decay using the GEMINI++ model.

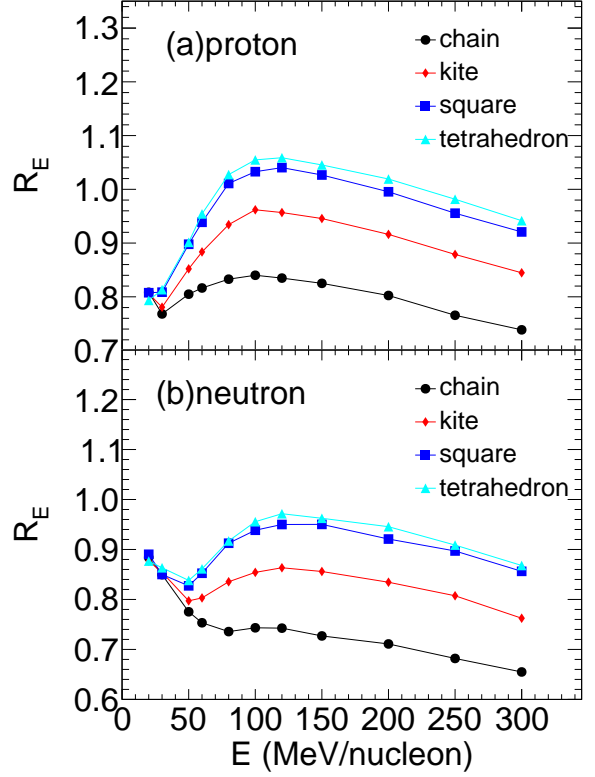


FIG. 1. The stopping R_E of proton and neutron as a function of beam energy.

As displayed in Fig. 1, one can find that the stopping power R_E of neutrons and protons is sensitive to nuclear clustering structures. For these four configurations, the stopping power follows a hierarchy tetrahedron $>$ square $>$ kite $>$ chain. From the geometric arrangement, we know that the tetrahedron configuration is more compact than the chain configuration. The more compact the structure, the higher the central density and thus, the greater the nuclear stopping power. This also implies that there is a corresponding order of compactness among these four configurations: tetrahedron $>$ square $>$ kite $>$ chain. Interestingly, it is found that this hierarchy of nuclear stopping is the opposite of the order of fragment fluctuations [69–71], which are represented by double ratios of light nuclei, namely proton, deuteron, triton or ^4He [30], indicating an inverse relationship between nuclear stopping and fragment fluctuations. In Fig. 1, we also note that in the 20–50 MeV/nucleon range, the neutron R_E decreases with increasing energy. This is consistent with experimental results [9]. In the reference, the cause responds to the strong decrease of the fusion cross section in this bombarding energy range [9, 72]. Here,

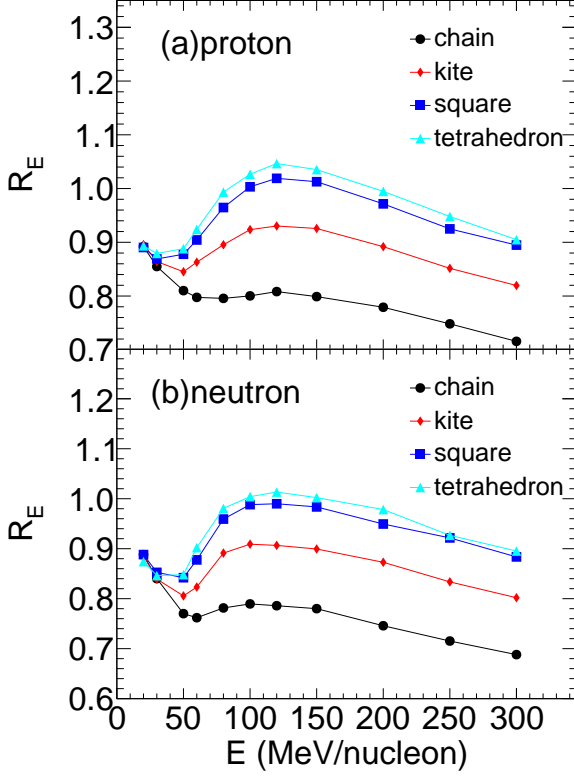


FIG. 2. The same as Fig. 1, but without Coulomb interaction.

we also consider an intrinsic reason: at this low energy region, the mean field and Pauli blocking dominate, and the increase in energy leads to an increase in the repulsive potential. When the compressional impact reaches its maximum, it tends to expand in the direction of the beam. This reduces the transfer of transverse momentum into longitudinal one, which means a smaller R_E .

However, for protons, no decreasing trend is observed in the 20-50 MeV/nucleon range even though the neutron-proton symmetric projectile and target system is used in this work. The main reason for this difference is due to Coulomb interactions. To verify this, in Fig. 2, we turn off the Coulomb interaction, and it can be seen that both the proton and neutron R_E exhibit a decreasing behavior in the 20-50 MeV/nucleon range. There is also no longer a distinction in the magnitude of R_E .

As the energy increases, two-body collisions increase, leading to an increase in R_E . Here, it can be seen that for the square and tetrahedron configurations, their values exceed 1. This indicates that in this energy regime, there is strong squeeze-out, with enhanced emission at polar angles of 90° [22]. Moreover, with a further increase in collision energy, R_E decreases. The decrease in R_E is due to the reduction of the cross section. In the model, the collision cross section is described by Eq.(11). From the equation, it is clear that as the collision energy increases, the collision cross section decreases, which in turn leads

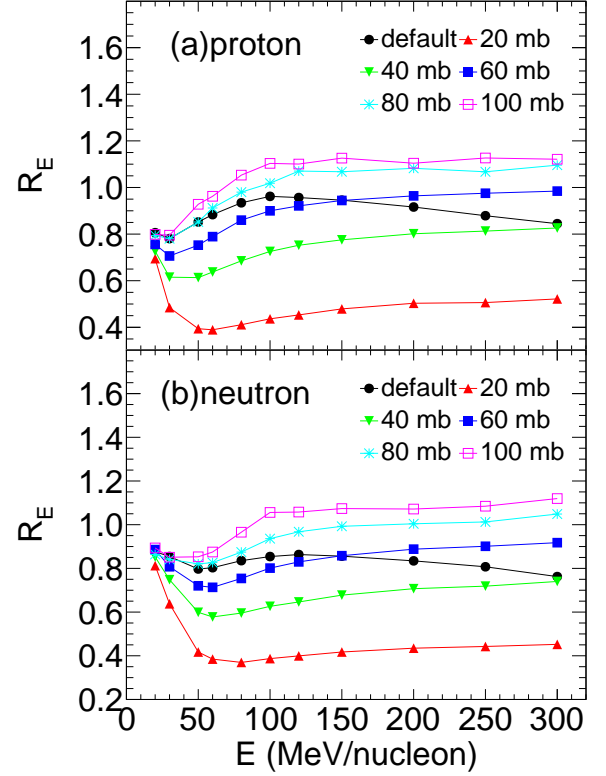


FIG. 3. The R_E as a function of beam energy for protons and neutrons at different collision cross sections using the kite configuration.

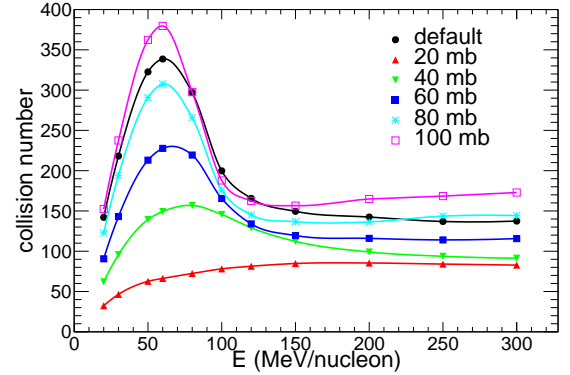


FIG. 4. The number of collisions as a function of beam energy for the kite configuration under different collision cross sections.

to a decrease in R_E . To illustrate this, we performed simulations with different cross-sections. As shown in Fig. 3, at high collision energies, the stopping power increases with the increase in cross-section. Only with the default cross-section form does the stopping show a decreasing trend. Furthermore, we also present the dependence of the number of collisions on energy for different cross-sections, as shown in Fig. 4. For the same reaction

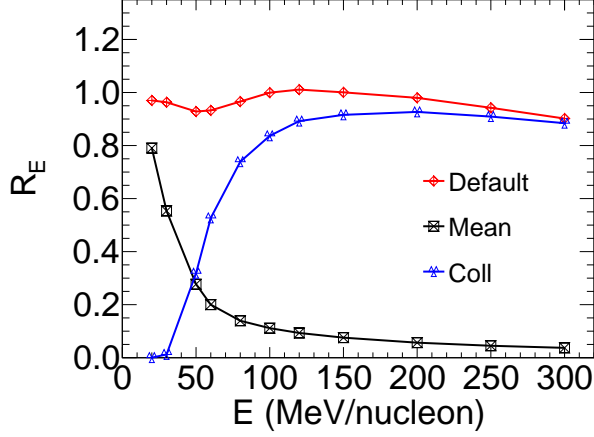


FIG. 5. The R_E as a function of beam energy for the tetrahedron configuration with different modes: Default (red curve), Mean: only mean field (blue curve), and Coll: cascade (black curve).

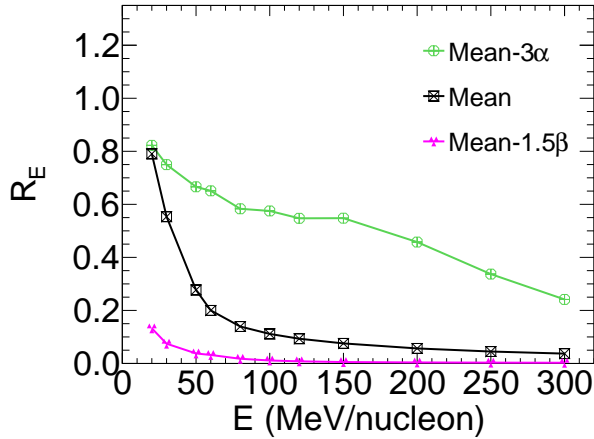


FIG. 6. The R_E as a function of beam energy for the tetrahedron configuration with different modes: Mean- 3α : only mean field with 3α (green curve); Mean: only mean field (black curve), and Mean- 1.5β : only mean field with 1.5β (pink curve).

energy, different collision cross sections lead to significant differences in the number of collisions. In general, a larger cross-section corresponds to a higher number of collisions. When the cross-section is large, the number of collisions first increases and then decreases. The maximum number of collisions indicates that the system has reached collision saturation. However, as the collision energy increases, the reaction time of the collision system decreases, leading to a reduction in the number of collisions. For small cross-sections, such as 20 mb, saturation is not reached. The energy point corresponding to the maximum value of R_E does not coincide with the energy

point where the number of collisions is maximal. This implies that there is no strong correlation between the number of collisions and the stopping power.

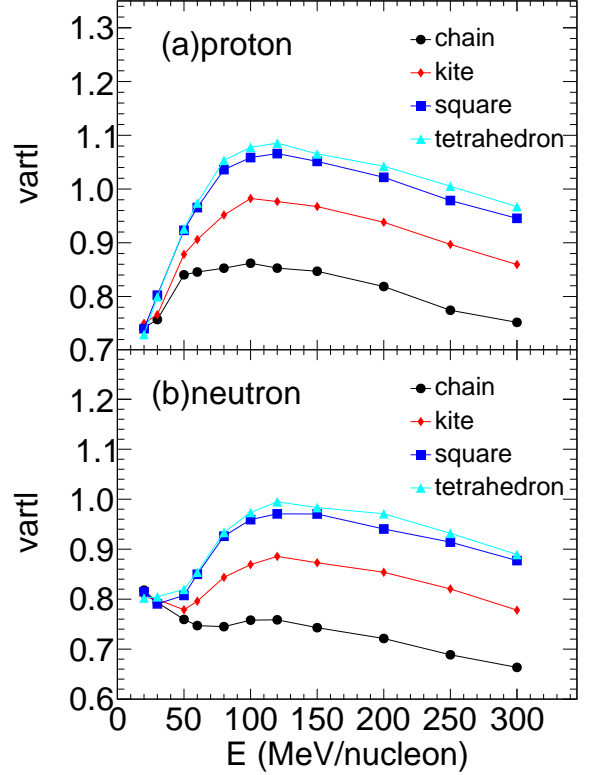


FIG. 7. The $vartl$ of proton and neutron as a function of beam energy for different configurations.

Additionally, we have tried to use some simplified modes as in Figs. 5 and 6. Note that since the fragment is unavailable in such modes, R_E in Figs. 5 and 6 are extracted from the nucleon space. Figure. 5 presents the energy dependence of R_E for three different modes: Default, Mean: only mean field and Coll: only cascade, i.e. mean-field is turned off and only collision term remains. It can be seen that when only the mean field is considered, R_E monotonically decreases as energy increases. In the cascade mode, however, R_E first increases with energy and then shows a decreasing trend. This suggests that the decrease of R_E at high energies is not only due to the effect of the cross-section, but the mean field also plays a role. As in Fig. 6, we enlarge the parameters α and β , which correspond to attractive and repulsive interactions in Eq. (6), by multiplying them by 3.0 and 1.5, respectively. Figure. 6 shows that when the attractive interaction increases, the stopping power increases. In contrast, when the repulsive interaction is increased, the stopping power decreases.

Finally, the another stopping observable is also presented, namely observable $vartl$ as the Eq. (20), which is also related to the R_E . As shown in Fig. 7, $vartl$ is similar to R_E as in Fig. 1. Essentially, here $vartl$ shows

similar sensitivity to the different cluster configurations as R_E does in Fig. 1, indicating the robust finding for the relationship of nuclear stopping versus the clustering configurations.

IV. CONCLUSIONS

This study used the EQMD model to investigate how nuclear cluster configurations affect the stopping power R_E in central $^{16}\text{O}+^{40}\text{Ca}$ collisions. The stopping power was found to be sensitive to the cluster structure, with the tetrahedral configuration exhibiting the highest stopping power, followed by the square, kite and chain configurations. More compact structures with higher central densities resulted in higher stopping power. Perhaps we cannot really determine the exact structure of a nucleus, but we may be able to probe the initial state of the nucleus — whether it is compact or diffuse — through the magnitude of the stopping power. Neutron stopping power decreased in the 20-50 MeV/nucleon range, while proton stopping power was affected by Coulomb interactions. At higher energies, two-body collisions initially increase the stopping power, but it decreases as the collision cross section decreases. The study also showed that

the number of collisions correlates with the cross section, but not directly with the stopping power. Both mean field and cascade processes were found to influence the energy dependence of stopping power. Finally, changes in attractive and repulsive interactions affected stopping power, with attractive interactions increasing it and repulsive interactions decreasing it. These results improve our understanding of the role of nuclear cluster configurations and interactions on stopping power in heavy-ion collisions.

ACKNOWLEDGMENTS

The authors thank Dr. Chen Zhong for maintaining the high-quality performance of Fudan HIRG supercomputing platform for nuclear physics. This work received partial support from the National Key R&D Program of China Nos. 2023YFA1606701, the National Natural Science Foundation of China under Contract Nos. 12147101, 12205049, 12347149, 11890714, and 11925502, the Strategic Priority Research Program of CAS under Grant No. XDB34000000, the Guangdong Major Project of Basic and Applied Basic Research No. 2020B0301030008, and the STCSM under Grant No. 23590780100.

-
- [1] J. M. Lattimer, M. Prakash, *Phys. Rep.* **621**, 127 (2016).
 - [2] B. A. Li, C. M. Ko, W. Bauer, *Int. J. Mod. Phys. E* **7**, 147 (1998).
 - [3] G. F. Bertsch and S. Das Gupta, *Phys. Rep.* **160**, 189 (1988).
 - [4] J. Aichelin, *Phys. Rep.* **202**, 233 (1991).
 - [5] M. O. Kuttan *et al.*, *Phys. Rev. Lett.* **131**, 202303 (2023).
 - [6] L. G. Pang, X. N. Wang, *Nucl. Sci. Tech.* **34**, 194 (2023).
 - [7] W. B. He, Q. F. Li, Y. G. Ma *et al.*, *Science China Phys. Mech. Astro.* **66**, 282001 (2023).
 - [8] J. Zhou, and J. Xu, *Sci. Phys. Phys. Mech. Astro.* **67**, 282011 (2024).
 - [9] G. Lehaut *et al.* (INDRA and ALADIN Collaborations), *Phys. Rev. Lett.* **104**, 232701 (2010).
 - [10] G. Q. Zhang, Y. G. Ma, X. G. Cao *et al.*, *Phys. Rev. C* **84**, 034612 (2011).
 - [11] Y. D. Song, R. Wang, Z. Zhang and Y. G. Ma, *Phys. Rev. C* **108**, 064603 (2023).
 - [12] Y. G. Ma, *Journal of Fudan University (Natural Science)* **62**, 273 (2023).
 - [13] Y. Y. Liu, J. P. Yang, Y. J. Wang *et al.*, *Nucl. Sci. Tech.* **36**, 45 (2025).
 - [14] C. W. Ma, H. L. Wei, X. Q. Liu *et al.*, *Prog. Part. Nucl. Phys.* **121**, 103911 (2021).
 - [15] R. K. Puri, Y. G. Ma, A. Sharma (eds.), *Multifragmentation in Heavy-Ion reactions, Theory and Experiments*, Stanford Publishing, Singapore, 2024; ISBN: 978-981-4968-69-0.
 - [16] V. Baran, M. Colonna, V. Greco *et al.*, *Phys. Rep.* **410**, 335 (2005).
 - [17] A. Ono, *Prog. Part. Nucl. Phys.* **105**, 139–179 (2022).
 - [18] H. Wolter, M. Colonna, D. Cozma *et al.*, *Prog. Part. Nucl. Phys.* **125**, 103962 (2022).
 - [19] A. Sorensen, K. Agarwal, K. W. Brown *et al.*, *Prog. Part. Nucl. Phys.* **134**, 104080 (2024).
 - [20] X. G. Deng, D. Q. Fang, Y. G. Ma, *Prog. Part. Nucl. Phys.* **136**, 104095 (2024).
 - [21] B. A. Li, L. W. Chen, C. M. Ko, *Phys. Rep.* **464**, 113 (2008).
 - [22] W. Reisdorf, A. Andronic, A. Gobbi *et al.*, *Phys. Rev. Lett.* **92**, 232301 (2004).
 - [23] O. Lopez, D. Durand, G. Lehaut *et al.*, *Phys. Rev. C* **90**, 064602 (2014).
 - [24] M. D. Cozma, *Phys. Rev. C* **110**, 064911 (2024).
 - [25] D. Sharma and S. Kumar, *J. Phys. G: Nucl. Part. Phys.* **51**, 055102 (2024).
 - [26] Y. X. Zhang, Z. X. Li, and P. Danielewicz, *Phys. Rev. C* **75**, 034615 (2007).
 - [27] H. L. Liu, Y. G. Ma, A. Bonasera *et al.*, *Phys. Rev. C* **96**, 064604 (2017).
 - [28] Y. G. Ma, S. Zhang, *Influence of Nuclear Structure in Relativistic Heavy-Ion Collisions*. In *Handbook of Nuclear Physics*, I. Tanihata, H. Toki, T. Kajino (eds), Singapore.
 - [29] C. C. Guo, W. B. He, Y. G. Ma, *Chin. Phys. Lett.* **34**, 092101 (2017).
 - [30] Y. T. Cao, X. G. Deng, and Y. G. Ma, *Phys. Rev. C* **108**, 024610 (2023).
 - [31] K. Wei, Y. L. Ye, Z. H. Yang, *Nucl. Sci. Tech.* **35**, 216 (2024).
 - [32] P. Bożek, W. Broniowski, E. Ruiz Arriola, and M. Rybczyński, *Phys. Rev. C* **90**, 064902 (2014).

- [33] S. Zhang, Y. G. Ma, J. H. Chen *et al.*, [Phys. Rev. C **95**, 064904 \(2017\)](#).
- [34] S. Zhang, Y. G. Ma, J. H. Chen *et al.*, [Eur. Phys. J. A **54**, 161 \(2018\)](#).
- [35] Y. Y. Wang, S. Zhao, B. Cao *et al.*, [Phys. Rev. C **109**, L051904 \(2024\)](#).
- [36] Fei Li, Yu-Gang Ma, Song Zhang, Guo-Liang Ma, Qiye Shou, [Phys. Rev. C **106**, 014906 \(2022\)](#).
- [37] Chunjian Zhang, Jiangyong Jia, [Phys. Rev. Lett. **128**, 022301 \(2022\)](#).
- [38] Jiangyong Jia, Giuliano Giacalone, Chunjian Zhang, [Phys. Rev. Lett. **131**, 022301 \(2023\)](#).
- [39] Wouter Ryssens, Giuliano Giacalone, Björn Schenke, Chun Shen, [Phys. Rev. Lett. **130**, 212302 \(2023\)](#).
- [40] Jiangyong Jia, Giuliano Giacalone, Chunjian Zhang, [Chin. Phys. Lett. **40**, 042501 \(2023\)](#).
- [41] Fei Li, Song Zhang, Kai-Jia Sun, Yu-Gang Ma, [Phys. Rev. C **109**, 064912 \(2024\)](#).
- [42] Hao-jie Xu, Jie Zhao, Fuqiang Wang, [Phys. Rev. Lett. **132**, 262301 \(2024\)](#).
- [43] Chunjian Zhang, Jinhui Chen, Giuliano Giacalone, Shengli Huang, Jiangyong Jia, Yu-Gang Ma, [Phys. Lett. B **862**, 139322 \(2025\)](#).
- [44] Giuliano Giacalone, Wenbin Zhao, Benjamin Bally *et al.*, [Phys. Rev. Lett. **134**, 082301 \(2025\)](#).
- [45] B. Schenke, [Nucl. Sci. Tech. **35**, 115 \(2024\)](#).
- [46] J. F. Wang, H. J. Xu, F. Q. Wang, [Nucl. Sci. Tech. **35**, 108 \(2024\)](#).
- [47] M. I. Abdulhamid, B. E. Aboona, J. Adam *et al.* (STAR Collaboration), [Nature **635**, 67–72 \(2024\)](#).
- [48] G. Giacalone, [Nucl. Sci. Tech. **35**, 218 \(2024\)](#).
- [49] J. Y. Jia, G. Giacalone, B. Bally *et al.*, [Nucl. Sci. Tech. **35**, 220 \(2024\)](#).
- [50] J. B. Natowitz, G. Röpke, S. Typel *et al.*, [Phys. Rev. Lett. **104**, 202501 \(2010\)](#).
- [51] L. Qin, K. Hagel, R. Wada *et al.*, [Phys. Rev. Lett. **108**, 172701 \(2012\)](#).
- [52] T. Maruyama, K. Niita, and A. Iwamoto, [Phys. Rev. C **53**, 297 \(1996\)](#).
- [53] J. Aichelin and H. Stöcker, [Phys. Lett. B **176**, 14 \(1986\)](#).
- [54] C. Z. Shi, Y. G. Ma, X. G. Cao, D. Q. Fang, W. B. He, and C. Zhong, [Phys. Rev. C **102**, 014601 \(2020\)](#).
- [55] C. Z. Shi, X. Z. Cai, B. S. Huang, and Y. G. Ma, [Phys. Rev. C **109**, 054621 \(2024\)](#).
- [56] C. Z. Shi, X. Z. Cai, D. Q. Fang, and Y. G. Ma, [Eur. Phys. J. A **60**, 103 \(2024\)](#).
- [57] W. B. He, Y. G. Ma, X. G. Cao *et al.*, [Phys. Rev. Lett. **113**, 032506 \(2014\)](#).
- [58] Y. G. Ma, R. Wada, K. Hagel, M. Murray, J. S. Wang, L. J. Qin, A. Makeev, P. Smith, and J. B. Natowitz, [Phys. Rev. C **65**, 051602\(R\) \(2002\)](#).
- [59] R. J. Charity, in Joint ICTP-AIEA Advanced Workshop on Model Codes for Spallation Reactions (IAEA, Vienna, 2008), Report INDC(NDC)-0530.
- [60] R. J. Charity, [Phys. Rev. C **82**, 014610 \(2010\)](#).
- [61] R. J. Charity, M. A. McMahan, G. J. Wozniak *et al.*, [Nucl. Phys. A **483**, 371 \(1988\)](#).
- [62] W. Hauser and H. Feshbach, [Phys. Rev. **87**, 366 \(1952\)](#).
- [63] T. von Egidy and D. Bucurescu, [Phys. Rev. C **72**, 044311 \(2005\)](#); [Phys. Rev. C **73**, 049901\(E\) \(2006\)](#).
- [64] W. B. He, Y. G. Ma, X. G. Cao *et al.*, [Phys. Rev. C **94**, 014301 \(2016\)](#).
- [65] B. S. Huang, Y. G. Ma, W. B. He, [Eur. Phys. J. A **53**, 119 \(2017\)](#).
- [66] Chen-Chen Guo, Yu-Gang Ma, Zhen-Dong An, Bo-Song Huang, [Phys. Rev. C **99**, 044607 \(2019\)](#).
- [67] Yi-An Li, Song Zhang, and Yu-Gang Ma, [Phys. Rev. C **102**, 054907 \(2020\)](#).
- [68] Y. G. Ma, [Nucl. Tech. **46**, 080001 \(2023\)](#).
- [69] Kai-Jia Sun, Lie-Wen Chen, Che Ming Ko, Zhangbu Xu, [Phys. Lett. B **774**, 103–107 \(2017\)](#).
- [70] Xian-Gai Deng, Yu-Gang Ma, [Phys. Lett. B **888**, 135668 \(2020\)](#).
- [71] C. M. Ko, [Nucl. Sci. Tech. **34**, 80 \(2023\)](#).
- [72] P. Lautesse, L. Nalpas, R. Dayras *et al.* (INDRA Collaboration), [Eur. Phys. J. A **27**, 349-357 \(2006\)](#).